Published in Journal of the Optical Society of America A 22, issue 7, 1432-1441, 2005
which should be used for any reference to this work

Optical properties of microfabricated fully-metal-coated near-field probes in collection mode

Emiliano Descrovi, Luciana Vaccaro, Laure Aeschimann, Wataru Nakagawa, Urs Staufer, and Hans-Peter Herzig

Institute of Microtechnology, University of Neuchâtel, Rue A.-L. Breguet 2 and Rue Jaquet-Droz 1, 2000 Neuchâtel, Switzerland

A study of the optical properties of microfabricated, fully-metal-coated quartz probes collecting longitudinal and transverse optical fields is presented. The measurements are performed by raster scanning the focal plane of an objective, focusing azimuthally and radially polarized beams by use of two metal-coated quartz probes with different metal coatings. A quantitative estimation of the collection efficiencies and spatial resolutions in imaging both longitudinal and transverse fields is made. Longitudinally polarized fields are collected with a resolution approximately 1.5 times higher as compared with transversely polarized fields, and this behavior is almost independent of the roughness of the probe's metal coating. Moreover, the coating roughness is a critical parameter in the relative collection efficiency of the two field orientations.

1. INTRODUCTION

Apertureless scanning near-field optical microscopy probes were first proposed by Wickramasinghe and Williams[1] and subsequently developed by Zenhausern *et al.*,[2] where the probe was a standard silicon atomic force microscope (AFM) tip scattering the light transmitted through an illuminated sample. Subsequently, metal probes have also been employed for the same purpose. It was found that metallic tips scatter transversely and longitudinally polarized fields with different relative strengths.[3] In a previous paper[4] we reported a phenomenological description of a similar effect, taking place in the collection of light by apertureless microfabricated quartz probes.[5,6] There we also demonstrated that the collection efficiencies of the transverse and longitudinal fields are highly dependent on the roughness of the probe metal coating.

The aim of the present work is to complete the investigation on the polarization-dependent light-collection behavior of microfabricated quartz probes by quantifying and extending the previous findings. First, we give an experimental estimation of the relative collection efficiencies of transversely and longitudinally polarized fields. In addition, we demonstrate that the probe spatial resolution is significantly higher for collection of longitudinally versus transversely polarized fields.

The understanding of the coupling mechanism of nonparaxial polarized optical fields with metallic or fully metalized tips is an important topic in scanning near-field optical microscope (SNOM) imaging. As has been experimentally[7,8] and theoretically[9,10] demonstrated, the presence of a highly confined longitudinally polarized field at the apex of apertureless nanoprobes (used in the illumination-mode configuration) is responsible for obtaining images with superresolved features. Nevertheless, the complementary problem of the link between optical resolution and collection of transverse and longitudinal fields into apertureless transparent probes needs more investigation. To obtain information on the probe resolution for the two polarization directions, an experimental situation where the transverse and the longitudinal fields to be scanned are distributed over different regions of space is highly desirable. There are several ways of producing a longitudinally polarized field having little overlap with a transversely polarized field. One of the most elegant methods consists of focusing a radially polarized beam. In this case, a narrow on-axis longitudinally polarized peak arises on the optical axis, while a transversely polarized field surrounds it over an annular region.[11,12] The strength of the longitudinal field depends on the numerical aperture (NA) of the focusing lens and on the shape of the lens entrance pupil.[13] A focused azimuthally polarized beam is also exploited for comparison purposes: In the focal plane it has no longitudinal field component, and the transverse field is distributed in a ring-shaped pattern similar to that of the focused radially polarized beam. The collection of transverse and longitudinal fields is performed by raster scanning the focal plane of focused radially and azimuthally beams with the probe.

2. RADIALLY AND AZIMUTHALLY POLARIZED BEAMS GENERATED BY LIQUID-CRYSTAL ELEMENTS

In this section the generation and far-field characterization of the axially symmetric beams used in the experiment is described. Such beams can be produced in several ways (see, for example, Refs. 14–16). In the present setup two liquid-crystal (LC) cells are used.

A. Far-Field Measurements

The first element is the θ-cell polarization converter described in Refs. 17–19. The entrance and the exit plates of the cell are linearly and circularly rubbed, respectively. The direction of the linear rubbing on the entrance plate

determines the cell axis. Each LC molecule chain is characterized by a twist angle (i.e., the angle between the orientation of the molecules at the entrance and at the exit plates) that is a function of the angular position with respect to the cell axis. When the polarization-guiding conditions are met,[20] a linearly polarized beam incident on the entrance plate, propagating parallel to the θ-cell normal and with an electric field vector parallel or perpendicular to the cell axis,[21] experiences a rotation of its polarization direction by the twist angle. This phenomenon occurs for a broad range of wavelengths. However, in this case, a defect line running along the diameter parallel to the cell axis arises. The defect line is caused by the destructive interference of two opposite field contributions of equal amplitude over the same spatial region, as illustrated by Fig. 1. The defect line width is mainly determined by fabrication processes.

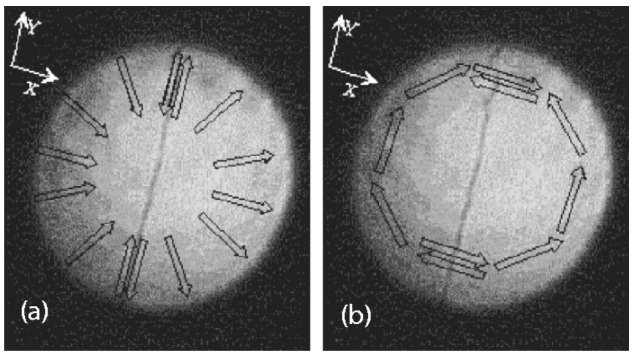

Fig. 1. Images of the incoming laser beam after passing through the θ cell, producing (a) an uncompensated radially polarized and (b) an uncompensated azimuthally polarized beam. Also note the presence of the defect line due to the destructive interference of the opposing polarization orientations in the two halves of the beam, as indicated schematically by the arrows.

In the following, the defintions of uncompensated radially and uncompensated azimuthally polarized beams will be used to indicate the two configurations displayed in Figs. 1(a) and 1(b), respectively. Note that, in this particular case, the input polarization is parallel to the θ-cell axis for the azimuthally polarized beam and perpendicular to it for the radially polarized one.

The axially symmetric beams generated by the θ cell are focused with an objective lens (NA=0.65). The focal-plane intensity distributions are imaged on a CCD by means of another microscope lens (NA=0.65). The uncompensated radial and uncompensated azimuthal configurations give rise to the same far-field pattern. As shown in Fig. 2, the transverse intensity distribution shows two reflection symmetries. By placing an analyzer in front of the CCD oriented either parallel or perpendicular to the input polarization, one finds either a fourfold or a three-lobed pattern, respectively. In conclusion, although the electric field vector lies along the radial or azimuthal direction, the θ cell does not provide the proper phase distribution for obtaining a circularly symmetric pattern in the focal plane of the lens. For this reason, the θ cell alone cannot be used in our setup, and a second element compensating for this effect is required.

To have axially symmetric beams with the desired phase distribution, we use a second LC plate. It is a phase-shifter cell providing a tunable phase delay between the two halves of the beam passing through it. It is

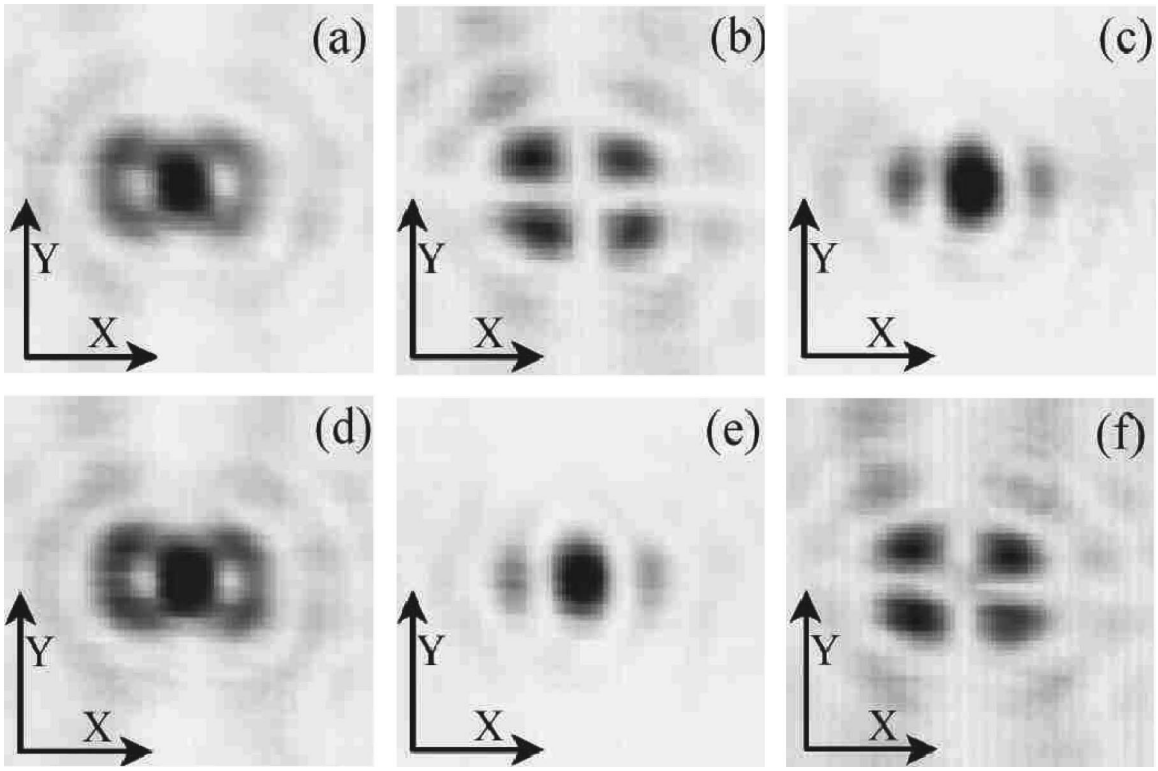

Fig. 2. Measured focal-plane images of uncompensated axially symmetric beams focused by a NA=0.65 objective. Azimuthally polarized beam: (a) total intensity, (b) intensity of the field x component, (c) intensity of the field y component. Radially polarized beam: (d) total transverse field intensity, (e) intensity of the field x component, (f) intensity of the field y component.

placed in the setup as depicted in Fig. 3. This LC element is composed of two glass substrates with a rubbed polyimide alignment layer. Structured transparent indium tin oxide electrodes define an active area of 1 cm × 1 cm. With a thickness of 6 μm and filled with the LC mixture BL006, the cell gives a retardation of 1772 nm at room temperature for parallel alignment. If voltage is applied, the retardation can be switched off. Since only the extraordinary index (n_e) is modulated, the input linear polarization should be aligned along this direction. As suggested in the drawing in Fig. 3, if a π-phase delay is applied to one half of the beam, then the output will be either a radially or an azimuthally polarized beam.

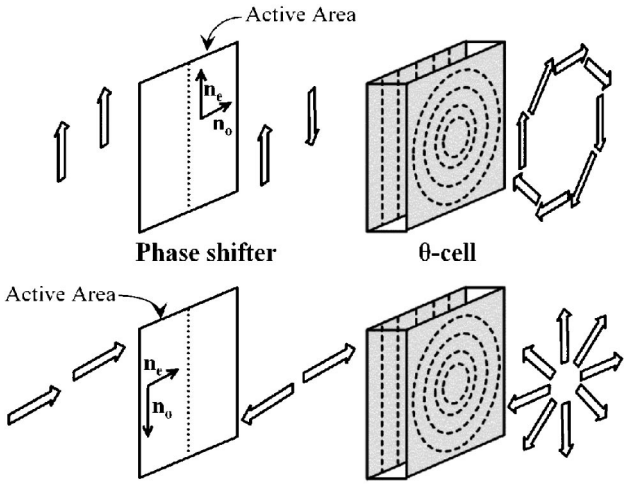

Fig. 3. Schematic drawing of the LiC elements generating axially symmetric polarized beams.

By focusing these beams, one finds intensity distributions having complete circular symmetry in the focal plane (Fig. 4). Rotational symmetry is also expected in the polarization distribution. If an analyzer oriented along an arbitrary direction θ with respect to the cell axis is placed in front of the CCD, the observed pattern is a two-lobed intensity distribution. The orientation of the lobes follows the polarization state of the beam as shown in Fig. 4. In general, axially symmetric linearly polarized beams can be described by the following Jones vector:[22]

$$\mathbf{J}_P = \begin{bmatrix} \cos(P\theta + \phi_0) \\ \sin(P\theta + \phi_0) \end{bmatrix}, \quad P = 1,2,3,\ldots. \tag{1}$$

In particular, the two beams produced as described above can be described by a Jones vector having $P=1$. In the following, they will be called compensated axially symmetric beams.

B. Comparison with Calculations

Calculations of the optical field distribution in the focal region of a thin perfect aplanatic lens have been performed. On the basis of the method described in Refs. 23–25, the implemented algorithm separately calculates each component of the **E**-field vector associated with a converging spherical wave as it propagates along the optical axis.

The following images present the results of calculations in which a NA=0.65 lens focuses a uniform field passing through an ideal θ cell and a lens pupil. In Fig. 5 the case

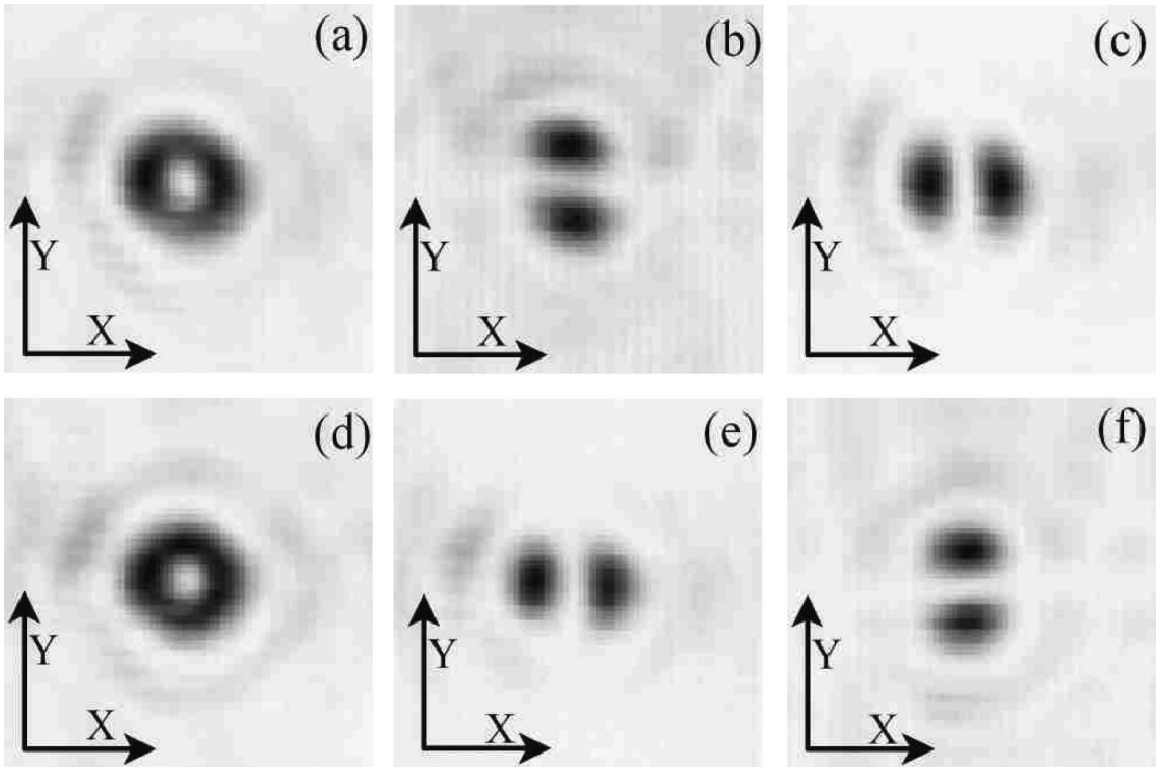

Fig. 4. Measured focal-plane images of compensated axially symmetric beams focused by a NA=0.65 objective. Azimuthally polarized beam: (a) total intensity, (b) intensity of the field x component, (c) intensity of the field y component. Radially polarized beam: (d) total transverse field intensity, (e) intensity of the field x component, (f) intensity of the field y component.

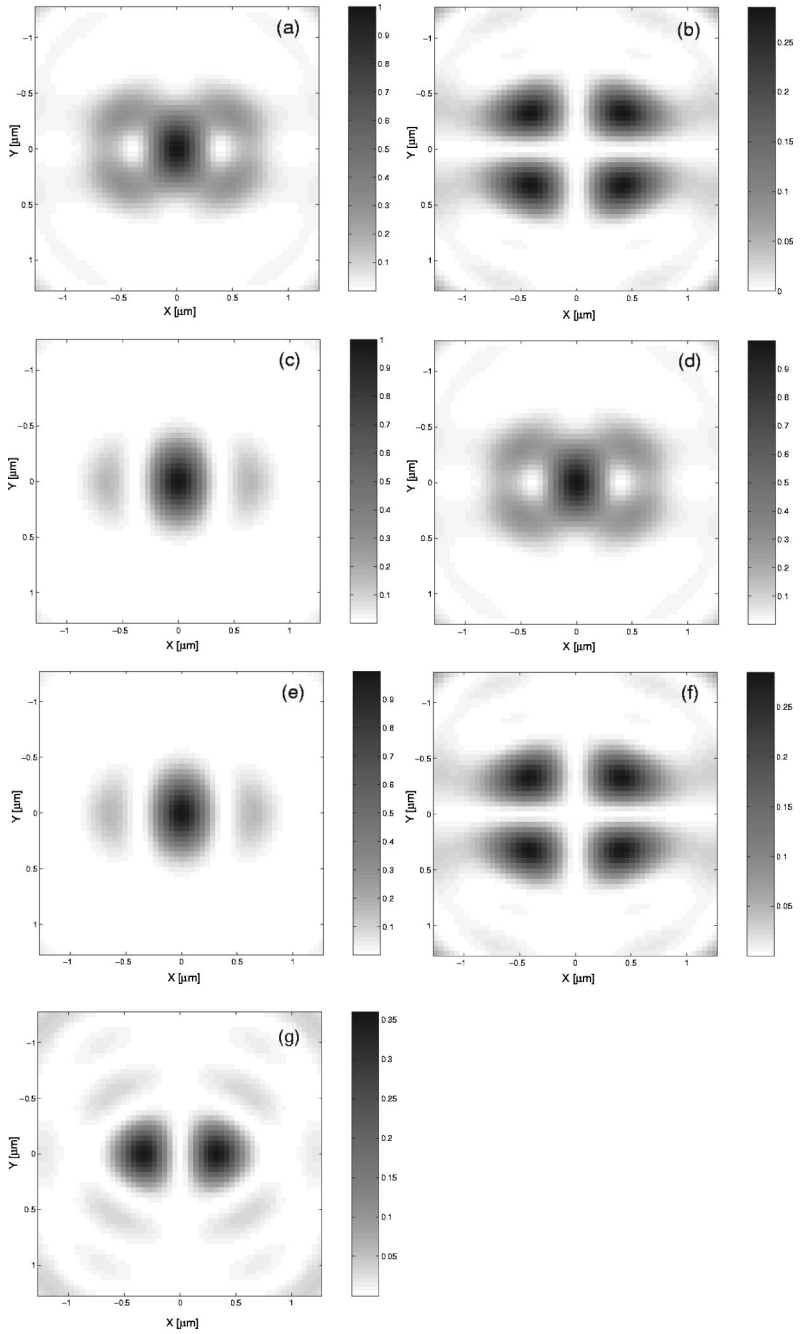

Fig. 5. Calculated patterns of uncompensated axially symmetric polarized beams produced by an ideal θ cell, in the focal plane of a NA=0.65 lens. Azimuthally polarized beam: (a) total intensity, (b) intensity of the field x component, (c) intensity of the field y component (the z component is zero). Radially polarized beam: (d) total transverse field intensity, (e) intensity of the field x component, (f) intensity of the field y component, (g) intensity of the field z component.

of the uncompensated beams is presented. The intensity patterns are normalized to the maximum value of the total intensity as the sum of all three Cartesian field components.

An analogous set of calculations for the compensated cases, where a π-phase delay is introduced in one half of the beam by an ideal phase-shifter plate, is shown in Fig. 6.

Calculations demonstrate that the transverse field (given by the sum of the x and y electric field components) for the two axially symmetric beams show similar patterns. This result is also confirmed by the far-field measurements shown previously. As already stated, only a focused radially polarized beam gives rise to a nonzero field z component. Since no significant difference is found between the collected focal-plane images of focused azimuthally and radially polarized beams, it is clear that the longitudinally polarized field is strongly attenuated in the image-formation process. This effect is quite well known and can be explained with simple geometrical considerations.[26] The calculated intensity patterns associated with the z component of the field will be further employed in the following sections for comparison with near-field images collected with the SNOM probes.

We conclude this section with some general remarks on axially symmetric beams. It is well known that, in the paraxial limit, the vectorial Helmholtz equation admits a family of beamlike solutions describing the transverse vectorial field with an inhomogeneous polarization state.[27,28] Such solutions are called Bessel–Gauss modes: In particular, the two lowest-order solutions represent azimuthally and radially polarized beams. In our experiment, since the two axially symmetric beams are created by a space-variant phase modulation of an incoming TEM_{00} mode, we cannot define them as pure Bessel–Gauss modes. Nevertheless, we underline that the ultimate aim of producing such beams is to focus them in order to obtain a certain polarization-dependent field distribution suitable for our investigation.

3. PROBE–FIELD INTERACTION

Once the axially symmetric beams are generated and focused, scans of the focal plane are performed with a collection-mode SNOM with microfabricated apertureless

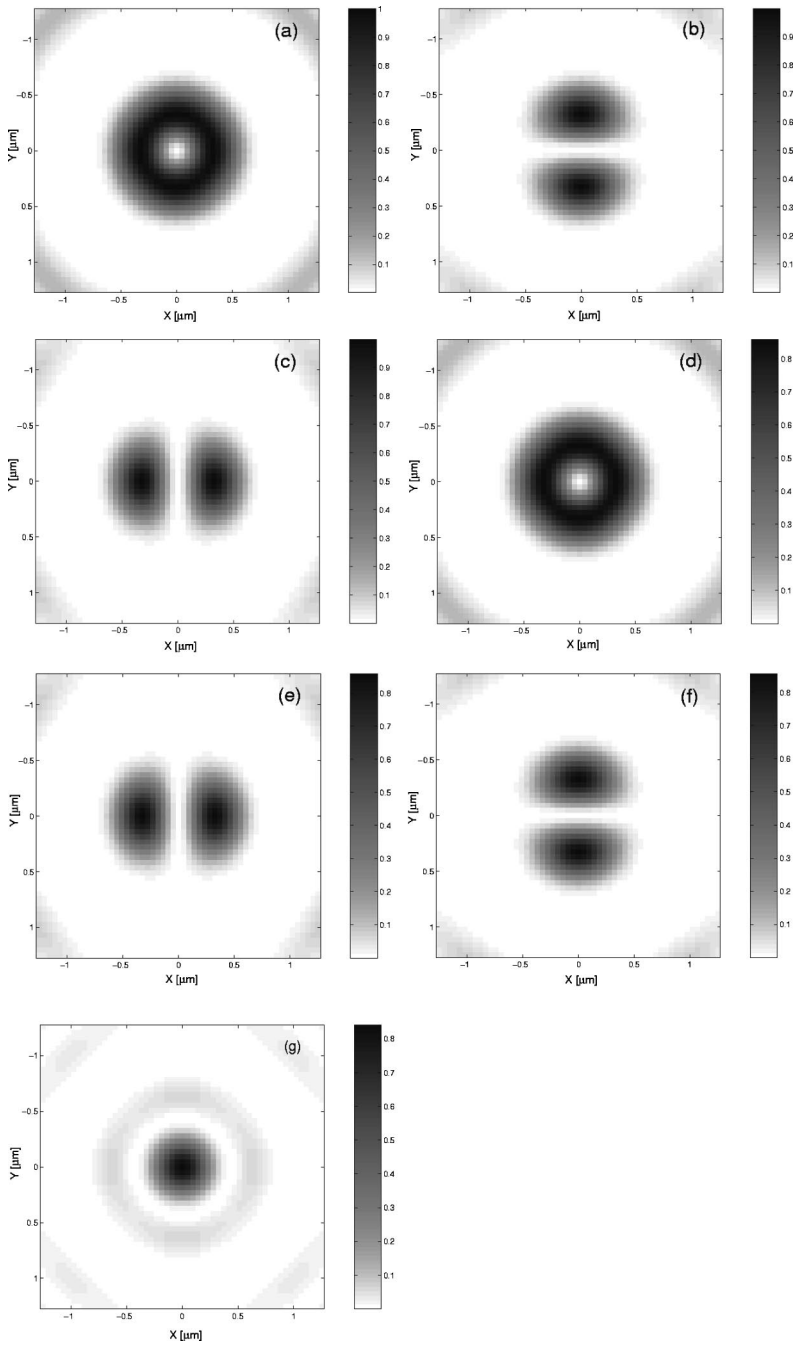

Fig. 6. Calculated patterns of compensated axially symmetric polarized beams produced by an ideal θ cell and focused with a NA = 0.65 lens. Azimuthally polarized beam: (a) total intensity, (b) intensity of the field x component, (c) intensity of the field y component (the z component is zero). Radially polarized beam: (d) total transverse field intensity, (e) intensity of the field x component, (f) intensity of the field y component, (g) intensity of the field z component.

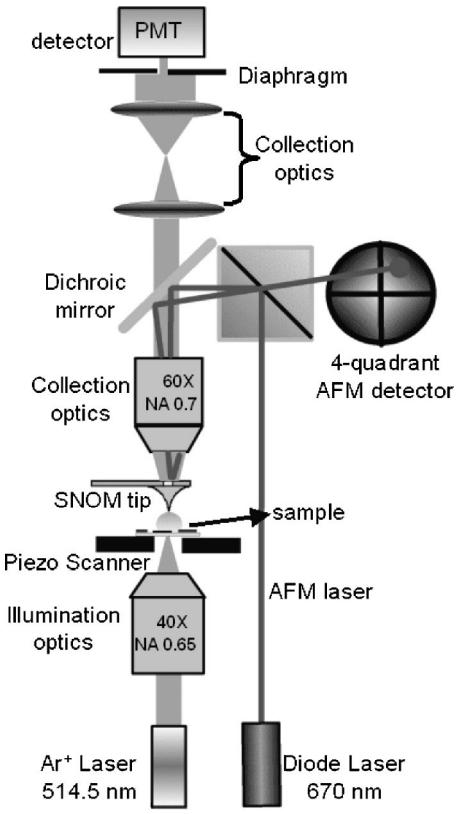

Fig. 7. Working principle of the SNOM used in the experiment. PMT, photomultiplier tube.

SiO_2 probes. The collection properties of two different probes having different metal-coating characteristics are presented and compared.

A. Near-Field Microscope

A schematic diagram of the apparatus is shown in Fig. 7. The device is a static AFM working as a collection-mode SNOM in transmission. In the present experiment, no samples are topographically scanned, and so the AFM system is not employed.

The laser source is an Ar^+ laser of 514.5 nm wavelength. The linearly polarized beam is converted into an axially polarized one by use of the two LC plates described previously. It is possible to switch from radial to azimuthal mode with a 90° rotation of the input polarization. The beam is then focused close to the tip by a lens (NA=0.65) mounted on the *xyz* piezostage (PiezoFlexure Stage P-517.3CL). The scans are performed by moving the piezostage in a plane (the focal plane of the lens) at a fixed distance from the SNOM head. The area of the scans is 2 μm$\times$2 μm. The light collected by the probe propagates through a square hole in the cantilever placed behind the tip base. With the help of some collection lenses and a diaphragm, an image of the hole in the photomultiplier photocathode plane (Perkin Elmer MD-952) is produced. A CCD is also employed for alignment purposes.

B. Compensated Azimuthally and Radially Polarized Beams Mapped with Standard Probes

The micromachined SNOM probes are 12 μm long amorphous SiO_2 tips integrated on silicon cantilevers.[5,6] They are completely coated with polycrystalline aluminium having a thicknness as great as 60 nm. The probe has no aperture at its apex and is circularly symmetric. A hole in the cantilever, located underneath the tip base, allows light to pass through. A detailed description of fabrication and characterization of standard probes can be found in Ref. 29.

The first kind of probe employed in the experiment (called the standard probe) is presented in Fig. 8. The aluminum coating is deposited in the step-coverage mode:[30] i.e., a method consisting of a rotation of the wafers in the planetary wafer holders in such a way that the metal is evaporated under a constantly varying angle. By evaporation of 100 nm of aluminium on the wafer, a uniform layer of approximately 60 nm thickness covers the tip entirely. Metal grains are formed during the deposition process, but they are contained in the coating layer. The estimated roughness of the metal layer is 1.9 nm$\pm$0.5 nm.

The focused compensated azimuthally polarized beam as imaged by the SNOM system with a standard probe is shown in Fig. 9(a). In Fig. 9(b) the recorded pattern of a focused compensated radially polarized beam is shown. The two measurements have been done in sequence, after the polarization of the input beam has been turned by 90°. The inhomogenities in the intensity distribution are mainly due to the quality of the beam.

The most important difference between the two images is in the amount of light detected in the neighborhood of the center of the annular pattern. This effect is attributed to the contribution of the longitudinal field present only in the case of the focused radially polarized beam. Therefore a portion of the longitudinal field component must be collected by the probe. To investigate this coupling effect more quantitatively, we analyze the intensity profiles measured along the dashed lines of Fig. 9. Along the chosen directions, the measured distributions display the

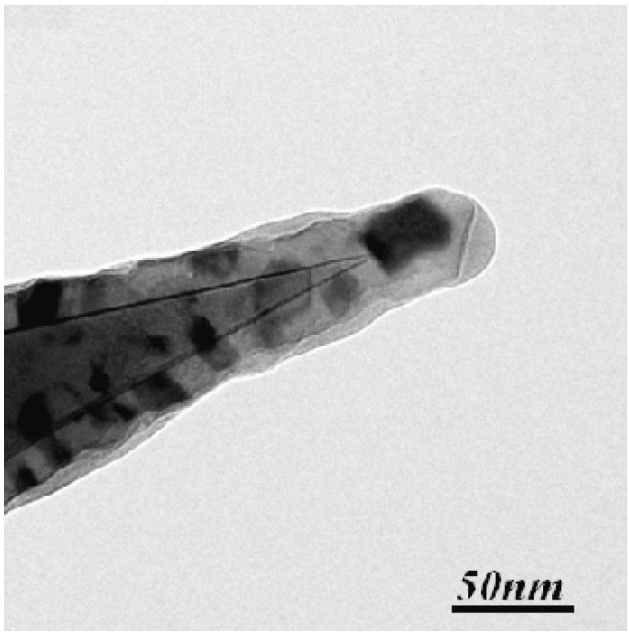

Fig. 8. Transmission electron microscope image of a SiO_2 tip coated with aluminum in the step-coverage mode (the standard probe).

best symmetry. A comparison with calculations is then performed as follows. The azimuthally polarized case is considered first. In this case a focal-plane field distribution whose polarization state is essentially transverse is expected.

To take into account the finite resolving power of the probe, we convolve the theoretical profile of the transverse field $\mathcal{I}_T$ with a Gaussian-shaped function $f_T = \exp[-(x^2/2\sigma_T^2)]$. The Gaussian is taken as the instrumental function of the microscope. This procedure is commonly applied in cases where the details of the probe–field interaction cannot be modeled in an accurate way (an example is found in Ref. 31). The parameter σ_T is determined by a least-squares fit of the measured data I^{azi} with the function $\mathcal{I}_T \circ f_T$. The best fit is obtained for $\sigma_T = 153$ nm. In Fig. 10 the measured data I^{azi}, the normalized theoretical profile $\mathcal{I}_T$, and the result of the convolution $\mathcal{I}_T \circ f_T$ are shown.

In the case of the radially polarized beam, since the polarization state of the pattern is not homogenous, both the longitudinal and the transverse field contributions must be taken into account, the total intensity being the sum of the two. In our analysis the following assumptions are made:

- The theoretical transverse $\mathcal{I}_T$ and longitudinal $\mathcal{I}_L$ components are individually convolved with two different Guassian functions, $f_T = \exp(-x^2/2\sigma_T^2)$ and $f_L = \exp[-(x^2/2\sigma_L^2)]$, respectively.
- The detected total intensity is given by a weighted sum of the longitudinal and transverse field contributions $I^{\text{rad}} = I_T^{\text{rad}} + CI_L^{\text{rad}}$. The value of C gives an indication of the ratio of the probe-collection efficiency for longitudinally polarized fields to that one for transversely polarized fields.

Furthermore, since in this particular case the images of the focused azimuthally and radially polarized beams are collected with the same probe, we assume that the collection behavior of the tip with respect to the transverse component of the field is the same in both measurements. Thus we apply the same value of σ_T in both the radial and the azimuthal cases. A two-parameter least-squares fit of data with the function $\mathcal{I}_T \circ f_T + C(\mathcal{I}_L \circ f_L)$ is performed, which searches for the best values of σ_L and C. The results are reported in Fig. 11, where the measured points I^{rad}, the theoretical profile $\mathcal{I}_T + \mathcal{I}_L$, and the weighted sum of the convolved profiles $\mathcal{I}_T \circ f_T + C(\mathcal{I}_L \circ f_L)$ are shown. The optimal values are $\sigma_L = 102$ nm and $C = 27.3\%$. We note that the root mean squares of the microscope instrument functions for the two field orientations are significantly different, with the transverse Gaussian $f_T(\sigma_T = 153$ nm) being significantly broader than the longitudinal Gaussian $f_L(\sigma_L = 102$ nm).

C. Compensated Azimuthally and Radially Polarized Beams Mapped with Rough Probes

The second kind of probe used in the experiment is coated by use of a different process (see Fig. 12). In this case the aluminium has been deposited in the normal mode: The wafers are not rotated during the evaporation procedure, so the metal is deposited normally to the wafer surface. The result is a chaotic distribution of small metal grains and a much higher roughness (5.5 nm ± 0.5 nm) than in

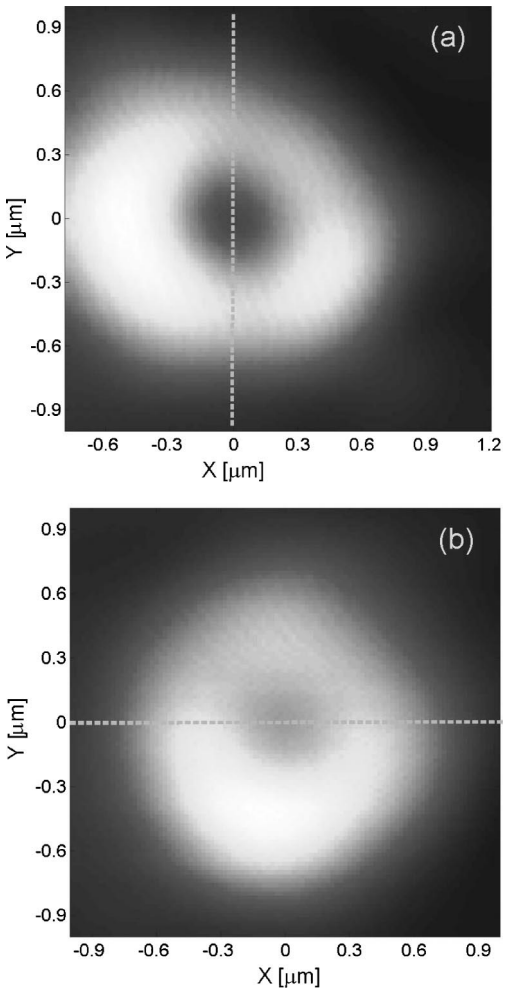

Fig. 9. Intensity distribution of a focused compensated (a) azimuthally polarized beam and (b) radially polarized beam scanned by the SNOM with a standard probe.

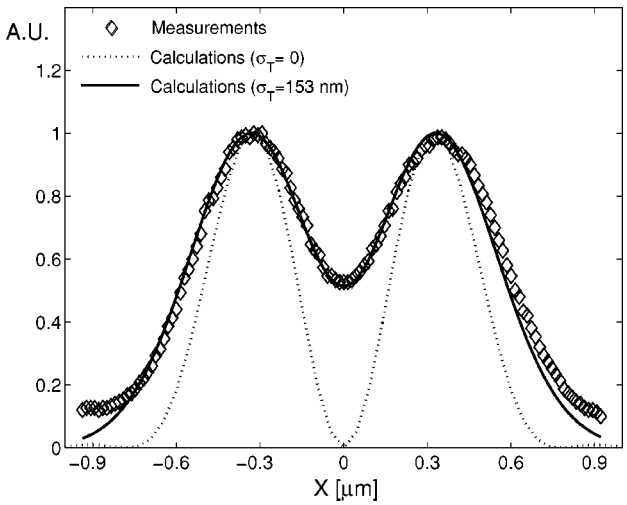

Fig. 10. Intensity profile of a compensated focused azimuthally polarized beam. The curves show the measured data I^{azi} (diamonds), the theoretical distribution $\mathcal{I}_T$ (dotted curve), and the convolution $\mathcal{I}_T \circ f_T$, with $\sigma_T = 153$ nm (solid curve). The measured profile is taken along the dashed line shown in Fig. 9(a).

the case of a standard probe. This kind of probe will be called the rough probe in the following.

We consider again the focused azimuthally polarized beam. The detected image is shown in Fig. 13(a) and shows a pattern similar to the calculated one.

The intensity distribution of the radially polarized beam, shown in Fig. 13(b), is then considered. The image looks completely different from the results with the standard probe: A single spot rather than a ring-shaped pattern is found. A comparison with calculations reveals that the collected field is indeed distributed in the same way as the longitudinal field in the focal plane of a focused radially polarized beam.

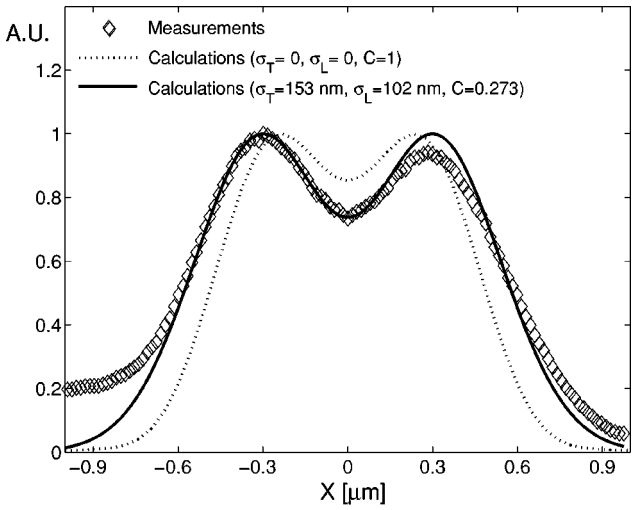

Fig. 11. Intensity profile of a compensated focused radially polarized beam. The curves show the measured data (diamonds), the theoretical distribution $\mathcal{I}_T+\mathcal{I}_L$ (dotted curve), and the weighted sum of the convolved distributions $\mathcal{I}_T\circ f_T+C(\mathcal{I}_L\circ f_L)$, with $C=0.273$ (solid curve). The measured profile is taken along the dashed line shown in Fig. 9(b).

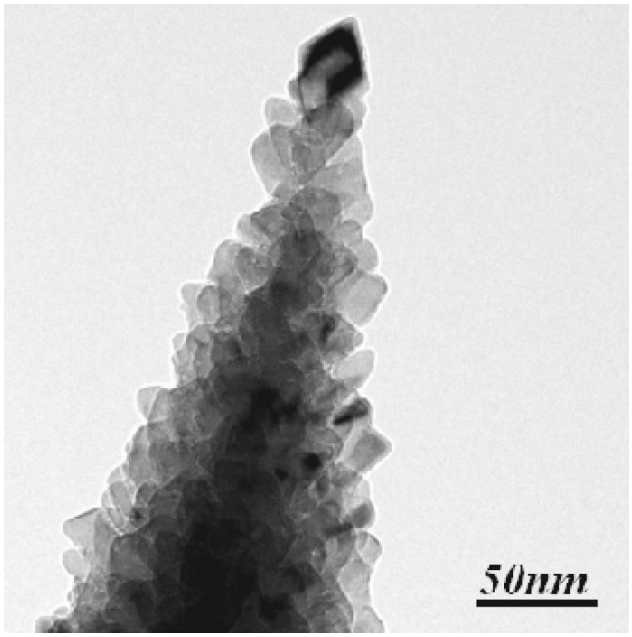

Fig. 12. Transmission electron microscope image of the apex of a SiO_2 tip coated with aluminum in the normal mode (the rough probe).

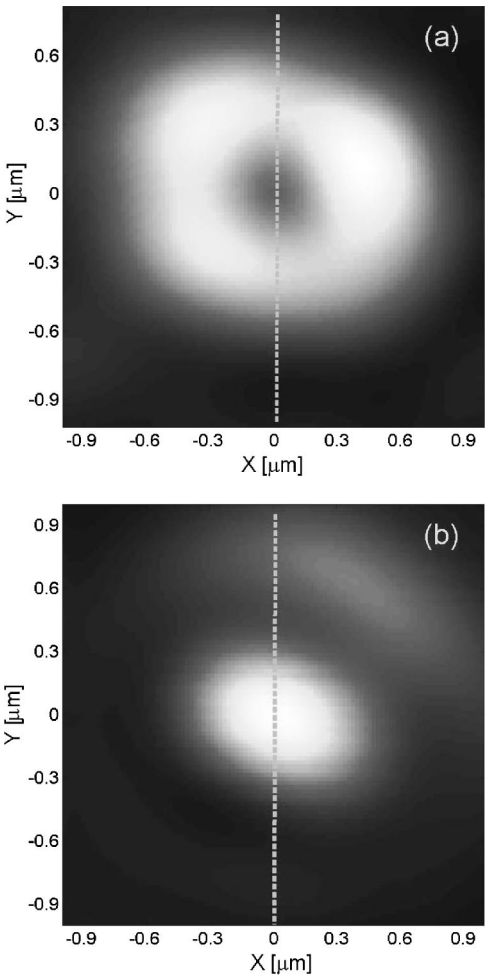

Fig. 13. Intensity distribution of a focused compensated (a) azimuthally polarized beam and (b) radially polarized beam as imaged by the SNOM with a rough probe.

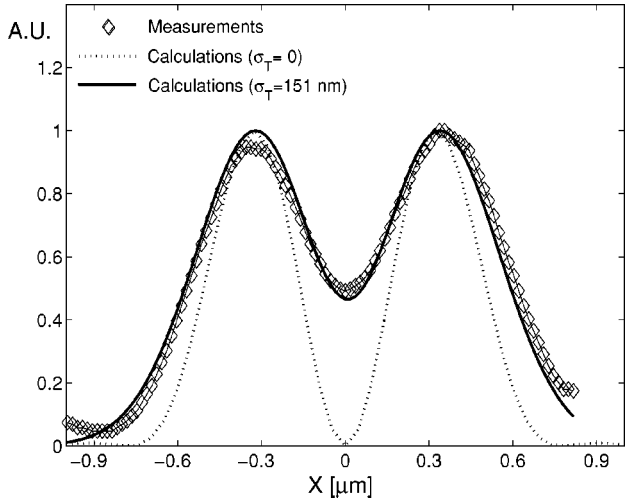

Fig. 14. Intensity profile of a compensated focused azimuthally polarized beam. The curves show the measured data I^{rad} (diamonds), the theoretical distribution $\mathcal{I}_T$ (dotted curve), and the convolution $\mathcal{I}_T\circ f_T$, with $\sigma_T=151$ nm (solid curve). The measured profile is taken along the dashed line shown in Fig. 13(a).

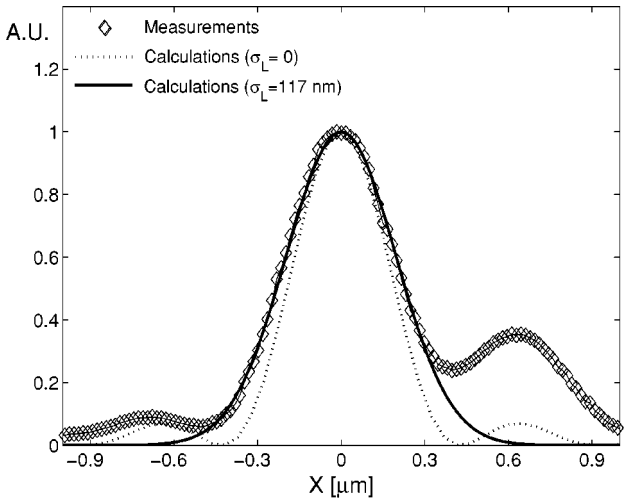

Fig. 15. Intensity profile of a compensated focused radially polarized beam. The curves show the measured data I^{rad} (diamonds), the theoretical distribution $\mathcal{I}_L$ (dotted curve), and the convolution $\mathcal{I}_L \circ f_L$, with $\sigma_L = 117$ nm (solid curve). The measured profile is taken along the dashed line shown in Fig. 13(b).

By taking the intensity cross section along the dashed lines in Fig. 13, we obtain the profiles shown in Figs. 14 and 15. In the azimuthal case a convolution with a Gaussian function f_T having σ_T as a free parameter is performed. The best fit is given by $\sigma_T = 151$ nm, a value very close to the one obtained for the standard probe. This indicates that the behavior of the two kinds of probe in collecting transverse fields is almost the same. In the radial case, for comparison purposes, we assume that only the longitudinal component has been collected by the probe. Consequently, the theoretical profile $\mathcal{I}_L$ of the longitudinal field distribution is convolved only with an instrument Gaussian function f_L characterized by a σ_L to be determined by fitting the experimental data I^{rad}. The results of the fitting processes give $\sigma_L = 117$ nm. Once again we find a narrower probe instrument function for the collection of longitudinal fields versus transverse fields.

4. DISCUSSION OF RESULTS AND CONCLUSIONS

The near-field optical microscope is nowadays one of the most promising tools for the investigation of the interaction of light with objects on a nanometric scale. It is known that, in such a situation, the description of optical fields in the paraxial approximation is clearly unsastisfactory and that the electromagnetic field must be considered in its whole vectorial nature. As a consequence, an understanding of the probe response with respect to the three-dimensional electromagnetic field becomes crucial. By considering the conical shape of the SNOM probe, we indentify two main polarization states that are of some interest to this end: parallel (longitudinal polarization) and perpendicular (transverse polarization) to the probe axis. In this paper we present for the first time, to our knowledge, an experimental determination of the relative collection efficiency and the relative spatial resolution that are obtained when these two fields are scanned and imaged by means of apertureless microfabricated quartz probes.

As the measurements performed with the rough probe demonstrate, we found that the value of $C = 27.3\%$ obtained for the standard probe is dramatically changed by altering the roughness of the metal coating. This effect can be explained by taking into consideration the light-guiding mechanism in the microfabricated probes as described in Ref. 4. In that work it was suggested that the coupling of transversely polarized light would take place at the probe sidewalls, as guided linearly polarized modes reach cutoff in the taper well before arriving at the probe apex. In the rough probe the roughness of the metal-coated sidewalls would then play a significant role in impeding the coupling of transversely polarized fields, resulting in a change of the collection efficiency ratio.

Another important collection property of microfabricated apertureless probes is the polarization-dependent resolving power. The Gaussian instrumental function used in the data fits is, in principle, related to the whole microscope system. Nevertheless, even if its value cannot be strictly considered a direct estimation of the spatial resolution of the probe, comparisons between different measurements performed with the same system can indeed be used to describe relative resolution performances. With the standard probe, we found a larger value of σ_T as compared with σ_L, and this trend is also found with the rough probe, where the values of σ_T and σ_L are very close to the standard probe case.

The previous results can be synthesized in the following three points: (1) the probe metal-coating roughness can dramatically affect the collection efficiency of transversely polarized fields but (2) has only slight influence on the resolution with which the two field orientations are imaged, and (3) longitudinally polarized fields are imaged with a higher resolution with respect to the transversely polarized fields. It is also interesting to note that, although the two kinds of probe used in the experiment clearly show different morphological characteristics, both of them possess a large metal grain (diameter ~40 nm) at the very apex of the tip. This observation, together with the results found in our experiment, suggests that this large grain could be primarily responsible for the collection of longitudinally polarized fields, which would be consequently coupled at the very apex of the probe. This conclusion also confirms the results of previous studies on the resolution properties of microfabricated apertureless SNOM probes used in an illumination-mode configuration,[8,10] where a connection between the observed high spatial resolution and longitudinally polarized fields confined at the probe apex was observed.

ACKNOWLEDGMENTS

The authors gratefully acknowledge T. Scharf and I. Philipoussis for the preparation of the liquid-crystal elements used in the experiment. This work has been supported by EU grant IST-2000-26479, the Swiss National Science Fundation, and the program TOP NANO 21.

E. Descrovi, the corresponding author, can be reached by e-mail at emiliano.descrovi@unine.ch.

REFERENCES

1. H. K. Wickramasinghe and C. C. Williams, "Apertureless near field optical microscope," U.S. patent 4,947,034 (April 28, 1989).
2. F. Zenhausern, M. P. O'Boyle, and H. K. Wickramasinghe, "Apertureless near-field optical microscope," Appl. Phys. Lett. **65**, 1623–1625 (1994).
3. A. Bouhelier, M. R. Beversluis, and L. Novotny, "Near-field scattering of longitudinal fields," Appl. Phys. Lett. **82**, 4596–4598 (2003).
4. E. Descrovi, L. Vaccaro, W. Nakagawa, L. Aeschimann, U. Staufer, and H. P. Herzig, "Collection of transverse and longitudinal fields by means of apertureless nanoprobes with different metal coating characteristics," Appl. Phys. Lett. **85**, 5340–5342 (2004).
5. G. Schürmann, W. Noell, U. Staufer, N. F. de Rooij, R. Eckert, J. M. Freyland, and H. Heinzelmann, "Fabrication and characterization of a silicon cantilever probe with an integrated quartz-glass (fused-silica) tip for scanning near-field optical microscopy," Appl. Opt. **40**, 5040–5045 (2001).
6. R. Eckert, J. M. Freyland, H. Gersen, H. Heinzelmann, G. Schürmann, W. Noell, U. Staufer, and N. F. de Rooji, "Near-field fluorescence imaging with 32 nm resolution based on microfabricated cantilevered probes," Appl. Phys. Lett. **77**, 3695–3697 (2000).
7. L. Novotny, E. J. Sanchez, and X. S. Xie, "Near-field optical imaging using metal tips illuminated by higher-order Hermite–Gaussian beams," Ultramicroscopy **71**, 21–29 (1998).
8. L. Aeschimann, L. Vaccaro, T. Akiyama, U. Staufer, N. F. de Rooij, R. Eckert, and H. Heinzelmann, "Polarization properties of fully metal coated scanning near-field optical microscopy probes," AIP Conf. Proc. **696**, 906–910 (2003).
9. A. Bouhelier, J. Renger, M. R. Beversluis, and L. Novotny, "Plasmon-coupled tip-enhanced near-field optical microscopy," J. Microsc. **210**, 220–224 (2002).
10. L. Vaccaro, L. Aeschimann, U. Staufer, H. P. Herzig, and R. Dändliker, "Propagation of the electromagnetic field in fully coated near-field optical probes," Appl. Phys. Lett. **83**, 584–586 (2003).
11. K. S. Youngworth and T. G. Brown, "Focusing of high numerical aperture cylindrical-vector beams," Opt. Express **7**, 77–87 (2000).
12. M. A. Lieb and A. J. Meixner, "A high numerical aperture parabolic mirror as imaging device for confocal microscopy," Opt. Express **8**, 458–474 (2001).
13. R. Dorn, S. Quabis, and G. Leuchs, "Sharper focus for a radially polarized light beam," Phys. Rev. Lett. **91**, 233901 (2003).
14. R. Oron, S. Blit, N. Davidson, A. A. Friesem, Z. Bomzom, and E. Hasman, "The formation of laser beams with pure azimuthal or radial polarization," Appl. Phys. Lett. **77**, 3322–3324 (2000).
15. Z. Bomzom, V. Kleiner, and E. Hasman, "Formation of radially and azimuthally polarized light using space-variant subwavelength metal stripe gratings," Appl. Phys. Lett. **79**, 1587–1598 (2001).
16. Z. Bomzon, G. Biener, V. Kleiner, and E. Hasman, "Radially and azimuthally polarized beams generated by space-variant dielectric subwavelength gratings," Opt. Lett. **27**, 285–287 (2002).
17. M. Stalder and M. Schadt, "Linearly polarized light with axial symmetry generated by liquid-crystal polarization converters," Opt. Lett. **21**, 1948–1950 (1996).
18. M. Stalder and M. Schadt, "Polarisation converters based on liquid crystal devices," Mol. Cryst. Liq. Cryst. Sci. Technol., Sect. A **282**, 343–353 (1996).
19. S. Masuda, T. Nose, R. Yamaguchi, and S. Sato, "Polarization-converting devices using a UV curable liquid crystal," in *International Symposium on Polarization Analysis and Applications to Device Technology*, T. Yoshizawa and H. Yokota, eds., Proc. SPIE **2873**, 301–304 (1996).
20. C. H. Gooch and H. A. Tarry, "The optical properties of twisted nematic liquid crystal structures with twist angles ≤90 degrees," J. Phys. D **8**, 1575–1584 (1975).
21. M. Schadt and W. Helfrich, "Voltage-dependent optical activity of a twisted nematic liquid crystal," Appl. Phys. Lett. **18**, 127–129 (1971).
22. R. C. Jones, "A new calculus for the treatment of optical systems," J. Opt. Soc. Am. **31**, 488–503 (1941).
23. M. Mansuripur, "Distribution of light at and near the focus of high-numerical-aperture objectives," J. Opt. Soc. Am. A **3**, 2086–2093 (1986).
24. M. Mansuripur, "Certain computational aspects of vector diffraction problems," J. Opt. Soc. Am. A **6**, 786–805 (1989).
25. M. Mansuripur, "Distribution of light at and near the focus of high-numerical-aperture objectives: erratum. Certain computational aspects of vector diffraction problems: erratum," J. Opt. Soc. Am. A **10**, 382–383 (1993).
26. T. Grosjean and D. Courjon, "Polarization filtering by imaging systems: effect on image structure," Phys. Rev. E **67**, 046611 (2003).
27. R. H. Jordan and D. G. Hall, "Free-space azimuthal paraxial wave equation: the azimuthal Bessel–Gauss beam solution," Opt. Lett. **19**, 427–429 (1994).
28. D. G. Hall, "Vector-beam solutions of Maxwell's wave equation," Opt. Lett. **21**, 9–11 (1995).
29. L. Aeschimann, T. Akiyama, U. Staufer, N. F. de Rooij, L. Thiery, R. Eckert, and H. Heinzelmann, "Characterization and fabrication of fully metal-coated scanning near-field optical microscopy SiO_2 tips," J. Microsc. **209**, 182–187 (2003).
30. M. Madou, *Fundamentals of Microfabrication* (CRC Press, Boca Raton, Fla., 1997).
31. P. Kramper, M. Kafesaki, C. M. Soukoulis, A. Birner, F. M. Gösele, U. Gösele, R. B. Wehspohn, J. Mlynek, and V. Sandoghdar, "Near-field visualization of light confinement in a photonic crystal microresonator," Opt. Lett. **29**, 174–176 (2004).